Drying-induced Atomic Structural Rearrangements in Sodium-based Calcium-alumino-silicate-hydrate Gel and the Mitigating Effects of ZrO_2 Nanoparticles

Journal:	*Physical Chemistry Chemical Physics*
Manuscript ID	CP-ART-11-2017-007876.R1
Article Type:	Paper
Date Submitted by the Author:	02-Mar-2018
Complete List of Authors:	yang, kengran; Princeton University, Özçelik, V. Ongun; Princeton University, Andlinger Center for Energy and the Environment Garg, Nishant; Princeton University, ; Gong, Kai; Princeton University, Department of Civil and Environmental Engineering White, Claire; Princeton University, Civil & Environmental Engineering

Drying-Induced Atomic Structural Rearrangements in Sodium-Based Calcium-Alumino-Silicate-Hydrate Gel and the Mitigating Effects of ZrO_2 Nanoparticles

Kengran Yang[1], V. Ongun Özçelik[1], Nishant Garg[1], Kai Gong[1] and Claire E. White[1]*

[1]Department of Civil & Environmental Engineering and Andlinger Center for Energy and the Environment, Princeton University, Princeton, USA

* Corresponding author: Phone: +1 609 258 6263, Fax: +1 609 258 2799, Email: whitece@princeton.edu

Postal address: Department of Civil & Environmental Engineering, Princeton University, Princeton NJ 08544, USA

Abstract

Conventional drying of colloidal materials and gels (including cement) can lead to detrimental effects due to the buildup of internal stresses as water evaporates from the nano/microscopic pores. However, the underlying nanoscopic alterations in these gel materials that are, in part, responsible for macroscopically-measured strain values, especially at low relative humidity, remain a topic of open debate in the literature. In this study, sodium-based calcium-alumino-silicate-hydrate (C-(N)-A-S-H) gel, the major binding phase of silicate-activated blast furnace

slag (one type of low-CO_2 cement), is investigated from a drying perspective, since it is known to suffer extensively from drying-induced microcracking. By employing *in situ* synchrotron X-ray total scattering measurements and pair distribution function (PDF) analysis we show that the significant contributing factor to the strain development in this material at extremely low relative humidity (0%) is the local atomic structural rearrangement of the C-(N)-A-S-H gel, including collapse of interlayer spacing and slight disintegration of the gel. Moreover, analysis of the medium range (1.0 – 2.2 nm) ordering in the PDF data reveals that the PDF-derived strain values are in much closer agreement (same order of magnitude) with the macroscopically measured strain data, compared to previous results based on reciprocal space X-ray diffraction data. From a mitigation standpoint, we show that small amounts of ZrO_2 nanoparticles are able to actively reinforce the structure of silicate-activated slag during drying, preventing atomic level strains from developing. Mechanistically, these nanoparticles induce growth of a silica-rich gel during drying, which, via density functional theory calculations, we show is attributed to the high surface reactivity of tetragonal ZrO_2.

Introduction

Drying is a common (and potentially detrimental) phenomenon seen in porous materials due to their interactions with the environment, as well as a processing technique used in a variety of industries, including sol-gel synthesis and ceramics. The removal of fluid (usually water) from a porous material can lead to a buildup of internal stresses.[1] Typically the body will not dry uniformly, and therefore a drying front will develop in the material where the dried outer component wants to shrink, whereas the moist interior restrains shrinkage. For composite

materials, differential shrinkage from drying can also occur internally in the material due to the presence of multiple phases, where restraint is provided by inclusions (phase(s) not susceptible to drying shrinkage). This mismatch in strain leads to tensile stresses developing on the surface of the material (if a drying front is present) or within the material (restrained shrinkage in vicinity of inclusions), and if these stresses exceed the tensile strength, the material will crack. Mitigation strategies include careful control of material thickness,[2] use of surface coatings to prevent cracking during evaporation[3] and controlled drying.[4] One class of material that is used in significant quantities around the world that is prone to suffer from drying, and therefore cracking, is concrete. Although there are several viable mediating technologies available for Portland cement-based concrete to prevent drying-induced microcracking, the underlying mechanisms responsible for the macroscopically-measured strains remain somewhat unclear, especially those occurring at low relative humidity (RH, < 40%). Moreover, the development of low-CO_2 cement alternatives, such as alkali-activated materials (AAMs), has led to a reexamination of cement degradation phenomena, including drying-induced microcracking.

Given that ordinary Portland cement (OPC) production accounts for 5 – 8% of anthropogenic CO_2 emissions,[5] there is a pressing need to develop and implement sustainable alternatives. AAMs are one of the most competitive alternatives, and have been shown to emit less CO_2 (~ 40 – 80%) compared with OPC.[6-8] AAMs utilize aluminosilicate-rich precursor materials, including industrial by-products such as ground granulated blast-furnace slag, fly ash from coal-fired power plants and calcined clays (e.g., metakaolin), which form mechanically hard binders (gels) when activated by alkaline solutions (or solids, as is the case for 1-part mixes[9,10]).[6,11] Furthermore, given correct mix designs, AAMs have comparable mechanical performance[12] and

cost[7] to OPC, and can be tuned to have superior properties via specific chemical compositions, such as high thermal performance[13] and low permeability.[14]

Nevertheless, questions remain regarding the long-term durability of AAMs, with the underlying degradation mechanisms often founded at the atomic/nanoscale, such as carbonation-induced chemical reactions[15-18] (from atmospheric and accelerated CO_2 conditions) and sulfate attack of the binder gel.[19,20] Progress is being made to elucidate the mechanisms responsible for chemical degradation of different types of AAMs, with the aim to pinpoint which mix designs are most resistant to different forms of degradation.[16,21,22] However, microcracking remains an outstanding durability and aesthetic issue for silicate-activated slag-based AAMs, and since silicate-activated slag possesses superior setting times,[23] strength development,[23] and permeability[14] compared with other AAMs, having a fundamental scientific understanding of the underlying cause(s) of microcracking is needed together with potential solutions for minimizing/mitigating this issue.

The susceptibility of silicate-activated slag to microcracking has been known for decades,[24-27] where the extent of microcracking in silicate-activated slag paste is considerably larger compared with OPC paste.[27] Collins and Sanjayan proposed that the difference in drying shrinkage between silicate-activated slag and OPC is due to their different pore size distributions, imposing different levels of capillary force on the OPC/silicate-activated slag paste as water is removed from the pores.[27] However, it is known that the pretreatment process (i.e., removal of pore liquid) required by the two major pore characterization techniques (i.e., nitrogen sorption and mercury intrusion porosimetry) may alter the pore structure of cementitious materials to a non-negligible extent.[28-33] More recently, based on the permeability results from the beam-bending technique, Scherer *et*

al. estimated the pore diameters of OPC paste to be ~ 1.5 – 5 nm,[28] which was also observed by Zeng *et al*. using nitrogen sorption with freeze-drying as the method of pretreatment.[34] Recent nitrogen sorption measurements on silicate-activated slag performed by Blyth *et al*.[14] with pretreatment via isopropanol solvent exchange showed that the major pore size obtained from the desorption curve of the isotherm is ~ 3 – 4 nm, which is close to that of OPC. However, it was also shown by Blyth *et al*. that the permeability of silicate-activated slag is lower than that of OPC paste (0.0001 nm^2 compared with 0.005 nm^2 at 7 days for water/precursor ratio of 0.5 (w/c ratio for OPC)).[14] As reported by Scherer, the permeability has an inverse relationship to the stresses that develop during drying,[35] and therefore, this difference in permeability between silicate-activated slag and OPC paste may be responsible in part for the susceptibility of silicate-activated slag paste to microcracking.

During drying of cementitious materials, it is generally accepted that there are no significant changes occurring to the atomic structure of the paste. Internal stresses lead to shrinkage of the body via consolidation of the particles (i.e., rearrangement of the cement grains). Only when the RH reaches very low levels (< 20%) does water evaporate from the interlayer spacing of calcium-silicate-hydrate (C-S-H) gel, the major binding phase of OPC paste, leading to a collapse of this interlayer spacing and an associated additional shrinkage at the macroscopic level.[36] However, a few articles have pointed to additional changes in the C-S-H gel structure due to drying, specifically intra- and inter-granular cohesion of C-S-H,[37] changes in the polymerization state of the silicate species[38] and a decrease in atomic ordering (as measured via the width of ^{29}Si nuclear magnetic resonance (NMR) peaks, with the proposed formation of new Ca-O-Si bonds as water is removed from the interlayer).[39] Additional research is required to

112 substantiate these results, and to uncover the link between these proposed changes and the
113 macroscopically measured drying shrinkage.
114
115 One experimental technique that is capable of probing the local atomic structure of
116 disordered/amorphous materials is pair distribution function (PDF) analysis. Using this
117 technique, we recently found that the atomic structure of sodium-containing calcium-alumino-
118 silicate-hydrate (C-(N)-A-S-H) gel in silicate-activated slag is more disordered (i.e., more
119 amorphous) than synthetic C-S-H gel, indicating that C-(N)-A-S-H gel may be
120 thermodynamically less stable.[40] Based on this observation, we hypothesize that the atomic
121 structure of C-(N)-A-S-H gel in silicate-activated slag may undergo atomic structural changes
122 (rearrangements) during drying, which contribute to the macroscopically measured drying
123 shrinkage at low RH values.
124
125 Here, we directly measure changes in the local atomic structure of silicate-activated slag *in situ*
126 as the material is subjected to drying conditions using synchrotron-based X-ray PDF analysis. By
127 tracking the evolution of specific atom-atom correlations we are able to quantify the extent of
128 change to the atomic structure as a function of RH, and also pin-point which atom-atom
129 correlations are affected by drying. Furthermore, we show it is possible to directly measure
130 drying-induced strain at the nanoscale via shifts of the higher *r* atom-atom correlations (between
131 10 and 22 Å), providing new insight on the susceptibility of C-(N)-A-S-H gel to undergo
132 alterations during drying.
133

To control/limit changes at the nanoscale in C-(N)-A-S-H gel during drying, we have investigated the impact of zirconia (ZrO_2) nanoparticles on the structure and stability of C-(N)-A-S-H gel, whose catalytic effect has been well documented.[41,42] Due to the high surface-to-volume ratio, nanoparticles may potentially improve the performance of cementitious materials by acting as extra nucleation sites for gel growth or providing a filler effect. Numerous studies have been conducted on adding nanoparticles to cementitious materials (albeit sometimes at extremely high concentrations (> 1% wt.) which may not be economically viable), revealing that the addition of nanoparticles can accelerate the hydration reaction process,[25,43-47] increase strength,[25,44,48,49] and reduce porosity.[25,48] However, there is limited literature available on the impact of nanoparticles on cementitious materials under drying conditions. Yang *et al*. reported that adding nano-TiO_2 in silicate-activated slag reduces the extent of drying shrinkage.[25] On the other hand, a review by Rashad showed that the addition of nano-silica to a cement-based mortar partially substituted by rice husk ash produced mix results for the extent of drying shrinkage.[50]

In this investigation, the impact of nano-ZrO_2 on the reaction kinetics of silicate-activated slag has been elucidated using *in situ* X-ray PDF analysis, together with the influence of these nanoparticles on the drying-induced changes that occur when silicate-activated slag is exposed to low RH environments. Nano-ZrO_2 was selected due to its high surface reactivity and stability under elevated pH conditions. Given that the nanoparticles are seen to drastically alter the nanoscale behavior of the material during drying, density functional theory (DFT) calculations have been used to uncover the mechanism by which the nanoparticle surfaces alter the evolution of the material during evaporation of the pore solution. The results provide new insight on the viability of using nano-ZrO_2 to limit the extent of drying-induced shrinkage strains in silicate-

157 activated slag, and therefore mitigate the extent of microcracking typically seen in these
158 sustainable cements.
159

160 Experimental

161 Material synthesis

162 Silicate-activated slag was synthesized using ground granulated blast-furnace slag (denoted as
163 slag), with the slag composition (GranCem, Holcim, specific gravity (SG): 2.89) shown in Table
164 1. The slag was activated using a sodium silicate solution with a Na_2O wt. % of 7 (i.e., 7g of
165 Na_2O per 100g of slag), since preliminary experiments showed that drying-induced
166 microcracking is prevalent at this alkali concentration. The sodium silicate solution was
167 synthesized by dissolving 13.8 wt. % of anhydrous sodium metasilicate (Na_2SiO_3, reagent grade,
168 Sigma-Aldrich, SG: 2.61) in deionized water. To ensure that the silicate species (i.e., oligomers)
169 in the solution reached equilibrium, the sodium silicate solution was mixed for at least 24 hrs
170 using a magnetic stirrer bar. The pastes were synthesized by manual mixing for ~ 2 min until the
171 samples appeared homogeneous. For the silicate-activated slag paste containing nano-ZrO_2,
172 0.167 wt. % (by mass of anhydrous slag) of ZrO_2 nanoparticles (supplied as a 10% wt. dispersion
173 in H_2O, Sigma-Aldrich, SG: 5.89) was added to the sodium silicate solution and stirred
174 thoroughly before the addition of slag powder. The average size of the ZrO_2 nanoparticles was
175 found to be 127.7 ± 2 nm, determined by dynamic light scattering. A detailed description of the
176 experiment and the size distribution of the nano-ZrO_2 can be found in the Electronic
177 Supplementary Information (ESI). The volume fraction of the nano-ZrO_2 in the mixture was

178 0.00033. The water-to-slag wt. ratio was set at 0.44 for all samples in order to maintain good
179 workability of the paste with and without the nano-ZrO_2.
180
181 After mixing, control samples (not exposed to drying conditions, one with and one without nano-
182 ZrO_2) were prepared by suctioning the paste into 1mm diameter polyimide capillary tubes using
183 a syringe. The two ends of the capillary were then sealed using quick-setting epoxy. These
184 control samples were measured at the start and end of the *in situ* drying measurements to assess
185 if the alkali-activation reaction contributed to the local atomic changes seen in the samples
186 exposed to drying conditions. The remaining pastes were sealed and left to cure for 24 hrs, after
187 which the samples were ground into fine powders using a mortar and pestle in a 96% RH glove
188 bag (using a K_2SO_4 saturated salt solution and N_2 gas), and then immediately loaded into
189 polyimide capillaries and sealed using porous glass wool in order to enable the nitrogen gas with
190 different RH to flow through the powdered samples during the *in situ* PDF measurements.
191
192 The RH of the gas used during the *in situ* PDF measurements was controlled by flowing dry N_2
193 gas through bubblers filled with different saturated salt solutions. Three different RH values were
194 used: 0% (using dry N_2 gas), 43% and 96%. The 43% and 96% RH conditions were attained by
195 using supersaturated K_2CO_3 and K_2SO_4 solutions, respectively (both from Sigma-Aldrich,
196 reagent grade).
197
198 Table 1. Oxide Composition (wt. %) of the slag used in this investigation. From ref. 15.

CaO	SiO_2	Al_2O_3	MgO	SO_3
42.5	34.5	11.7	7.3	1.7

199

200 **X-ray data collection and analysis**

201 The X-ray total scattering experiments were conducted at the Advanced Photon Source, Argonne
202 National Laboratory on the 11-ID-B beamline. The silicate-activated slag samples were mounted
203 and aligned in the gas cell[51] under ambient conditions. Each sample was analyzed using a
204 wavelength of 0.2112 Å and a two-dimensional image plate detector.[52] The detector-to-sample
205 distance was ~ 175 mm. For the samples exposed to drying conditions, a bubbler containing
206 mineral oil was connected to the gas cell arrangement to check for adequate gas flow through the
207 sample, and to indicate if a blockage had occurred. A pre-scan was conducted for each sample
208 for 10 min, where humid N_2 gas with 96% RH flowed through the sample. Afterwards, the gas
209 was switched to 0% or 43% RH, and data were acquired every 2.5 min. The duration of each test
210 was determined by screening data until no significant changes in the PDFs were observed. The
211 control sample was measured on the gas cell before and after each *in situ* drying measurement.
212 Data conversion from 2D to 1D was carried out using the program Fit2D with CeO_2 as the
213 calibration material.[53,54] The PDF, G(r), was obtained by taking a sine Fourier transform of the
214 measured total scattering function, S(Q), as shown in eqn. 1, where Q is the momentum transfer
215 given in eqn. 2.[55]

216 $$G(r) = \frac{2}{\pi}\int_{Q_{min}}^{Q_{max}} Q[S(Q) - 1]\sin(Qr)dQ \qquad (1)$$

217 $$Q = \frac{4\pi sin\theta}{\lambda} \qquad (2)$$

218 Standard data reduction procedures were followed to obtain the PDF using PDFgetX2,[56] with a
219 Q_{max} of 22 $Å^{-1}$.

220

The control silicate-activated slag samples (with and without nanoparticles) were also measured on 11-ID-B approximately five months after synthesis, in order to investigate the atomic changes due to the alkali-activation reaction. Due to slight differences in the beamline setup for the two experiments, a normalization procedure with respect to the photon count has been carried out for all data presented in this investigation.

Density functional theory calculations

DFT calculations were performed to compare the interaction energies of silicate ions (originating from the pore solution in the experiments) with different solid surfaces (zirconia vs. C-(N)-A-S-H present in the samples). These calculations were performed using the generalized gradient approximation (GGA) including van der Waals corrections.[57] The projector-augmented wave potentials (PAW) were used,[58] and the exchange-correlation potential was approximated with the Perdew-Burke-Ernzerhof functional.[59] The Brillouin zone was sampled using 5×5×3 *k*-points in the Monkhorst-Pack scheme where the convergence in energy as a function of the number of *k*-points was tested. The energy convergence value between two consecutive steps was chosen as 10^{-4} eV with an energy cutoff value of 500 eV. A maximum force of 0.05 eV/Å was allowed on each atom. The DFT calculations were carried out using the VASP software.[60]

Results & discussion

Impact of drying on C-(N)-A-S-H gel

Alterations to the local atomic structure

Figure 1 shows the PDF curves for the silicate-activated slag sample exposed to extreme drying conditions (0% RH, in Figure 1a) together with the data for the control sample (Figure 1b). Peak assignments given in Figure 1 are explained in detail in the Electronic Supplementary Information (ESI), where additional information on the local atomic structural changes seen during the alkali-activation reaction is provided. The PDF curves in Figure 1a have been normalized with respect to the maximum T-O peak intensity (T represents Si or Al) of the initial PDF data set at ~ 1.65 Å, since this nearest-neighbor bonding environment, specifically the number of tetrahedral Si/Al units in the sample, should be relatively constant throughout the drying process. A similar normalization process for PDF data has been used in our previous study.[61] The data from the control sample are not normalized because the experimental setup at 3624 h is slightly different from the rest, which may introduce artifacts in PDF peak intensities if normalization was carried out. The 0 hr data set in Figure 1a is defined as the start of 0% RH gas flow, at which point the silicate-activated slag control sample shown in Figure 1b has been curing for 24 hrs.

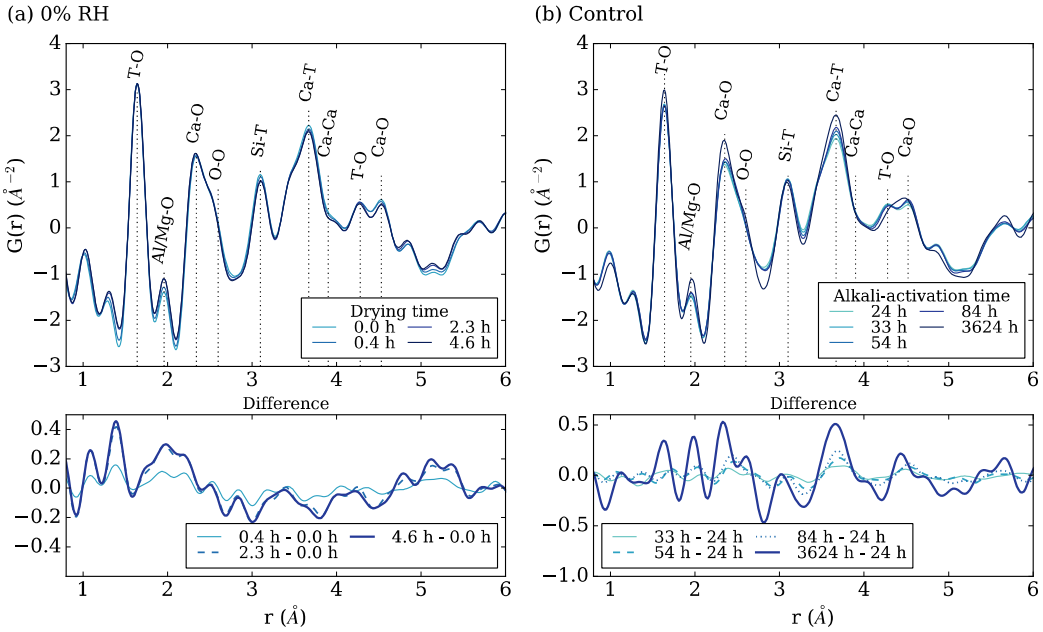

257

258 Figure 1. Synchrotron X-ray PDF curves of silicate-activated slag subjected to 0% RH (a), and
259 during the alkali-activation reaction (b, denoted as "control"). PDF curves at different times
260 during drying/alkali-activation (top), and difference curves of the PDF data obtained via
261 subtraction of the initial PDF data set (bottom).

262

263 It is clear from Figure 1 that the atomic structural changes that occur due to drying (Figure 1a)
264 are significantly different from the changes seen as a result of the alkali-activation reaction
265 (Figure 1b). The Ca-T correlation at ~3.65 Å, which provides an indication of the amount of C-
266 (N)-A-S-H gel in the sample,[15] is seen to decrease slightly with time in Figure 1a, which is
267 opposite to the trend in Figure 1b where the gel continues to precipitate throughout the course of
268 the measurement. The decrease of the Ca-Ca (at 3.90 Å) and Ca-O (at 4.53 Å) peak intensities in
269 Figure 1a implies that changes are occurring to the CaO layers (intra- or inter-layer Ca
270 environments) of the C-(N)-A-S-H gel. The Si-T correlation is observed to decrease in intensity

271 in Figure 1a, in contrast to Figure 1b where this peak does not change significantly during the
272 alkali-activation reaction.
273
274 Overall, the stark differences between Figure 1a and 1b show that there are observable changes
275 occurring in the atomic structure of silicate-activated slag during drying at 0% RH. The C-(N)-
276 A-S-H gel is experiencing rearrangements at the atomic length scale, where the Ca-O-T linkages
277 are being broken together with a decrease in the mean chain length (MCL) of the (alumino)silica
278 units or a reduction in the extent of cross-linking (seen via the loss of Si-O-T linkages). A
279 decrease in the MCL has also been observed in an OPC system with 22% wt. of slag and 22%
280 wt. of silica fume as supplementary cementitious materials by ^{29}Si NMR spectroscopy when
281 subjected to drying.[62] It is likely that as the interlayer water is being pulled out (which occurs
282 after the evaporation of the water from the gel pores), the large drying-induced capillary stresses
283 being exerted on the gel structure are high enough to cause bond breakage and subsequent
284 rearrangement at the atomic length scale. Hence, these data show that the atomic structure of C-
285 (N)-A-S-H gel likely undergoes disintegration to a certain degree as a result of exposure to
286 extreme drying conditions. Furthermore, by comparing the difference curve in Figure 1a with
287 PDF data in the literature on liquid water,[63,64] it is clear that the changes in the PDF curves of the
288 silicate-activated slag sample undergoing drying are not only due to the removal of water
289 molecules, but are also attributed to structural rearrangements of the atomic structure of silicate-
290 activated slag (for further discussion see ESI).
291
292 It has been recently reported in the literature that C-S-H gel in white Portland cement paste
293 undergoes nanoscale changes as a result of drying, where the small-angle X-ray scattering data

were fit using a disk-shaped model, and the data revealed that at low RH the disks reduce in thickness and width, which is in agreement with the slight disintegration-like behavior seen in Figure 1a.[65] On the other hand, the PDF curves for the silicate-activated slag sample exposed to moderate drying conditions (43% RH) do not show obvious changes in the atomic structure (see Figure S2a in ESI), and therefore disintegration of the C-(N)-A-S-H gel is only realized at extreme drying conditions.

Kinetics of local structural changes

To quantify the rate of change in the atomic structure of C-(N)-A-S-H gel as a result of drying (in both the 0% and 43% RH environments), two ratios have been calculated from peak intensities in the PDF data. It has been previously shown that the degree of polymerization of the C-(N)-A-S-H gel can be inferred from the maximum intensity of the Si-T correlation at ~ 3.1 Å divided by the intensity of the T-O peak at ~ 1.65 Å (i.e., (Si-T)÷(T-O)).[66] Likewise, information on the quantity of Ca-T linkages in the gel can be determined via (Ca-T)÷(T-O). The reason for dividing through by the T-O peak intensity is to account for any sample density increase/decrease that may occur due to the gas stream pushing powder in/out of the X-ray beam.

The (Si-T)÷(T-O) and (Ca-T)÷(T-O) ratios are given in Figure 2 for the samples exposed to 0 and 43% RH, together with these ratios for the control sample as the alkali-activation reaction evolves. After drying commences in the sample exposed to a 0% RH nitrogen gas flow, the (Si-T)÷(T-O) ratio is seen to continually decrease until equilibrium is reached after ~ 4 hrs. In contrast, the (Si-T)÷(T-O) ratios for the control sample and the sample exposed to 43% RH stay relatively stable during the measurement time frame (up to 9 hrs). Furthermore, the (Ca-T)÷(T-

O) ratio for the sample exposed to the 0% RH environment also shows a decreasing trend that is very similar to the (Si-T)÷(T-O) ratio trend. Hence, these data in Figure 2 provide quantitative evidence of the rearrangement of C-(N)-A-S-H gel, where breakage of the C-(N)-A-S-H gel structure involves segmentation along its elongated axis, where the (alumino)silica chains and CaO layers are seen to rupture simultaneously (Figure 3 shows this process schematically). Similar segmentation of a elongated C-S-H unit (~ 35 nm diameter, modeled as a disk shape) into shorter ones (~ 10 nm) below a RH of 40% was also identified in white Portland cement,[65] as mentioned earlier in this article. Moreover, we showed in a previous study that the nanoscale morphology of freeze-dried silicate-activated slag has a globular-like appearance as measured using helium ion microscopy, where the globules are of sizes ranging from ~10 to 100nm.[67] Although these globules are larger than the disk-like particle sizes obtained using small-angle scattering,[65] the helium ion microscopy data supports our hypothesis that the C-(N)-A-S-H gel undergoes a certain degree of disintegration due to exposure to extreme drying conditions.

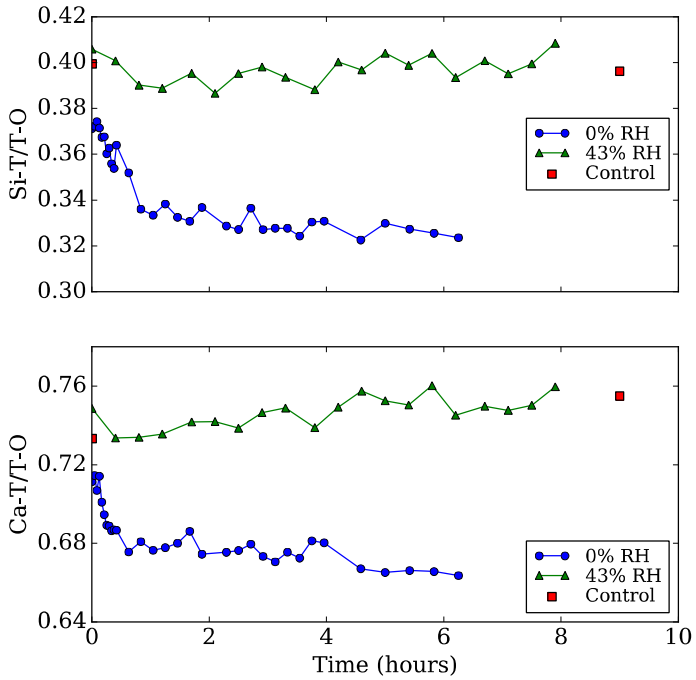

331

332 Figure 2. Evolution of normalized Si-T (at ~3.1 Å) and Ca-T (at ~3.65 Å) peak intensities of
333 silicate-activated slag at 0% RH, 43% RH and in the control (sealed) environment, all
334 normalized with respect to the T-O peak intensity at ~1.65 Å.

335

336 Based on the Kelvin equation, Jennings proposed that different mechanisms of drying operate at
337 different levels of RH.[68] At a RH of 0%, the interlayer spacing of the C-(N)-A-S-H gel will be
338 emptied, while pores of size 2 – 5 nm will be emptied at a RH of 40%.[68] In fact, a decrease in
339 basal (interlayer) spacing of the C-(N)-A-S-H atomic structure is observed in the reciprocal-
340 space diffraction data of the silicate-activated slag sample in the 0% RH environment (see Figure
341 S4a in the ESI), which has also been observed in C-S-H gel during drying using diffraction[69,70]
342 and molecular simulations.[36] However, the extent of change in the interlayer spacing of the C-S-
343 H gel is much larger (~ 2 Å)[69,70] than the amount measured in this study (0.6 Å, see ESI). This is

probably due to the difference in drying time, where our sample was dried for only a few hours, whereas the synthetic C-S-H samples were dried for a few weeks. The large difference in the amount of weight loss (more than 50% of the dried mass in the study by Gutteridge and Parrott[69] versus ~15% in our study (see ESI)) also supports this explanation.

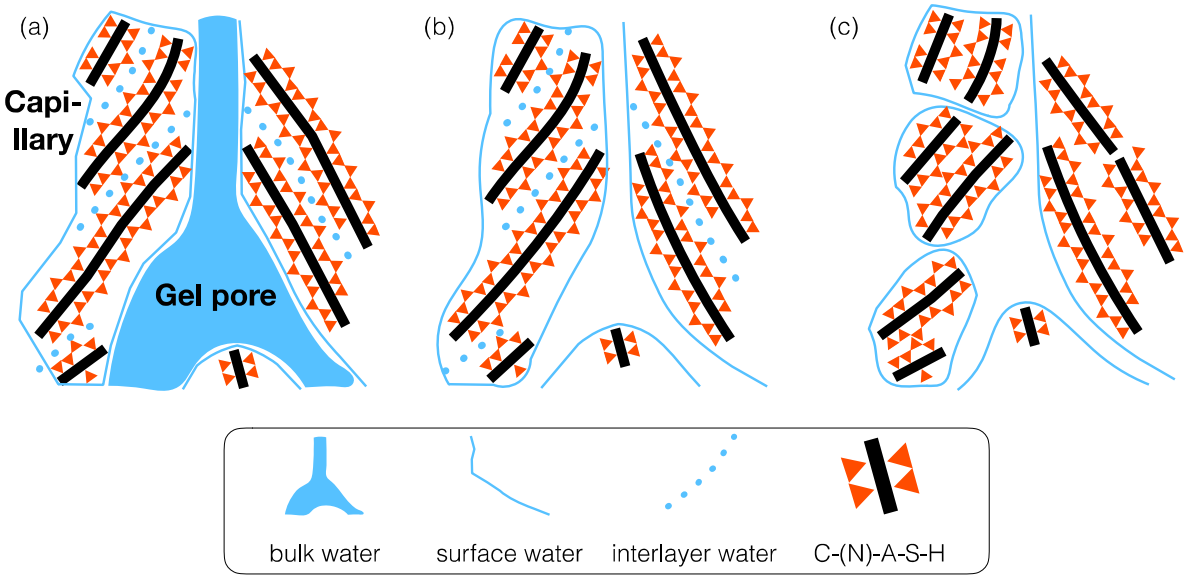

Figure 3. Schematic diagrams of C-(N)-A-S-H gel subjected to different RH at the nanoscale (~ 10 nm). (a) In the control environment, and (b) at 43% RH where only water in the gel pores is removed. (c) At 0% RH where all three types of water are removed (large C-(N)-A-S-H gel disintegrates into smaller ones, and its interlayer spacing decreases). The gel pores become smaller at smaller RH due to large capillary stresses being exerted on the material.

Strain at the nanoscale

The mid-range atomic ordering (10 – 22 Å) in the PDF data, as shown in Figure 4, contains information on the impact of drying on the interlayer collapse and associated development of

359 nanoscale strain in silicate-activated slag. Peak shifts at various *r* locations are found in the
360 silicate-activated slag subjected to the 0% RH drying condition, as indicated by the black arrows
361 in Figure 4a. However, shifts in the corresponding peaks in the silicate-activated slag subjected
362 to 43% RH are minimal, as shown in Figure 4b. Quantification of this observation is given in
363 Figure 5, where a summary of the extent of peak shifts is provided.
364

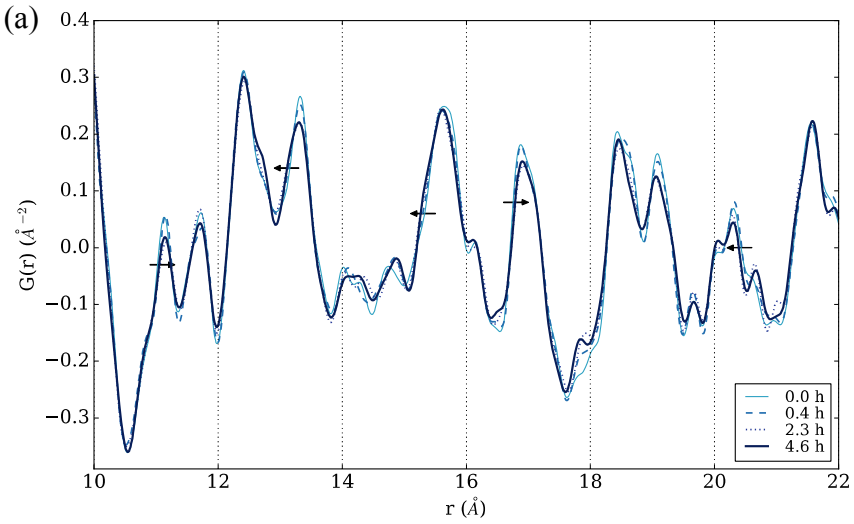

365

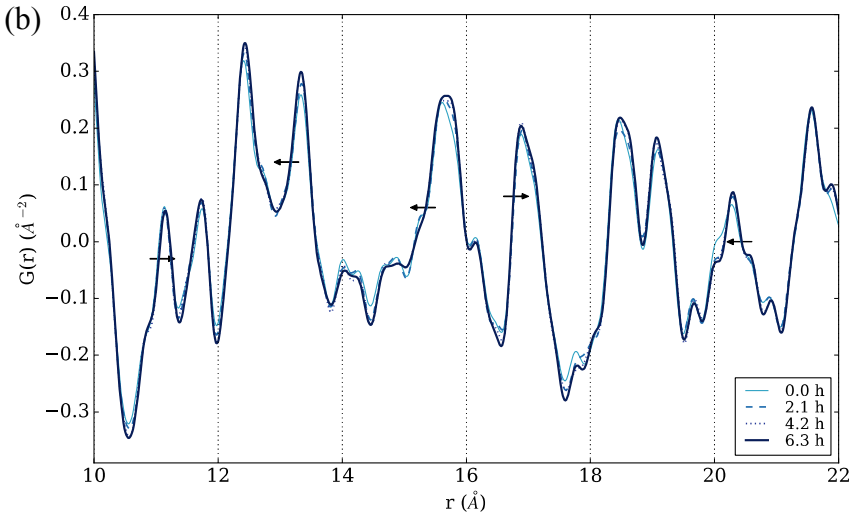

366

Figure 4. Synchrotron X-ray PDF curves of silicate-activated slag at (a) 0% RH and (b) 43% RH for different drying times, over an r range of $10 < r < 22$ Å. Black arrows indicate the direction of peak shifts for the case of 0% RH.

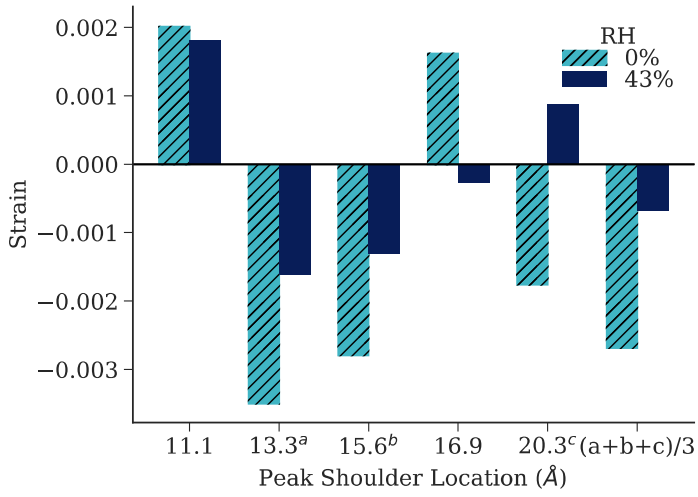

Figure 5. Quantification of the peak shifts in the PDF data for silicate-activated slag (Figure 4), given as strain values. A positive strain value indicates a shift of the peak shoulder towards larger atomic distances.

The extent of peak shift in the PDF data is represented using strain, defined as $(r_{end\ time} - r_{0\,h})/r_{0\,h}$, where $r_{0\,h}$ is the r position before drying and $r_{end\ time}$ is the r position after drying (i.e., $end\ time = 4.6\ h$ for 0% RH and $end\ time = 6.3\ h$ for 43% RH). For each peak, three intensity values (two for the peak at 20.3 Å because of its limited peak height) are selected along its shoulder, and the corresponding r values (atomic distances) are recorded, with the average value reported in Figure 5. It is clear from this figure that the magnitude of peak shift for the

382 silicate-activated slag in the 0% RH environment is larger than the 43% RH environment for all
383 five selected peaks.
384
385 It is anticipated that a collapse of the interlayer spacing in the C-(N)-A-S-H gel will be apparent
386 in the PDF data over an *r* range of 10 – 22 Å, assuming an initial interlayer spacing of ~ 11 – 14
387 Å. The peaks at 13.3, 15.6 and 20.3 Å in Figure 4 and Figure 5 do decrease in atomic distances,
388 however, the 11.1 and 16.9 Å peaks are seen to increase continually as drying progresses. Given
389 that the PDF data contain all atom-atom correlations in the material, the changes captured in
390 Figure 4 and Figure 5 will include not only quantitative information on the collapse of the
391 interlayer spacing, but also all other atomic structural rearrangements that occur during drying
392 (such as those associated with the disintegration as mentioned earlier, albeit manifested at a
393 longer length scale). However, teasing out the individual atom-atom correlations at this length
394 scale (10 – 22 Å) without an accurate structural model of C-(N)-A-S-H gel is extremely difficult.
395
396 The strain values presented in Figure 5 are within an order of magnitude of those measured at the
397 macroscopic level for pure C-S-H gel (0.03),[36,69] OPC paste (0.0005 to 0.003)[71,72] and previous
398 studies on silicate-activated slag (0.006)[25] and hydroxide-activated slag pastes (0.017).[70]
399 Interestingly, the excessively large strain values reported from XRD-measured changes in the
400 basal spacing for C-S-H gel (0.2),[36,69] which we also partially observe in the reciprocal space
401 data in the ESI for silicate-activated slag (0.6Å/14Å = 0.04) are not captured by the PDF data,
402 and therefore the PDF peak shifts better represent the magnitude of nanoscopic shrinkage that
403 occurs within the sample. The data presented in Figure 2 and 4b show that at 43% RH there are
404 limited changes occurring to the atomic structure of the C-(N)-A-S-H gel, and therefore the

corresponding strain values (Figure 5) are minimal (almost an order of magnitude smaller than those measured for 0% RH).

Many efforts have been made to link drying shrinkage of OPC observed at the macroscopic level with the underlying mechanisms originating at micro- and nanoscale. During the 1990's, Jennings and Xi identified knowledge gaps between the macroscopically measure drying strains and the underlying (and unresolved) multiscale mechanisms, and proposed a microscale model to help bridge this gap.[73,74] They used environmental scanning electron microscopy to provide experimental data for their model at the micron length scale, however, the strain measured using this technique was found to be 10 times larger than the macroscopic strain values.[73] Later, additional insight was provided by Thomas *et al.* using small-angle neutron scattering (SANS), where changes in the packing density and surface area of OPC were observed for different RH conditions.[75] They also noted that the SANS data was not able to elucidate information at the atomic level due to the resolution limit (in Q space) of the instrument.

Recently, Pinson *et al.* modeled the relationship between drying shrinkage and RH for OPC, where they attributed the macroscopic length change to three factors: Laplace pressure, surface energy and loss of interlayer water.[36] For the strain induced by the loss of interlayer water they assumed a simple linear relationship between the interlayer spacing and contributions to the macroscopic strain, where a scaling factor of 0.1 was applied to the extent of change of the basal spacing. This was carried out in light of the experimental results of Gutteridge and Parrott[69] and Neubauer *et al.*,[76] and Pinson *et al.* attributed such large differences in the nanoscopic and macroscopic strain values to the possibility that only part of the nanoscopic strain is

accommodated by the porous material and only some of the interlayer spaces undergo length changes. However, it is important to note that the basal spacing for C-S-H gel provides an average representation of interlayer spacing, and therefore if only part of the C-S-H underwent these changes, then the Bragg peak would not shift, but instead would broaden towards small *d* values (i.e., higher 2θ values). In fact, the XRD data provided in ref. 69 shows some signs of peak broadening, where a residual shoulder is present for the uncollapsed C-S-H interlayer spacing after drying. Hence, these data highlight the limitations of obtaining nanoscopic strain information from the shift of a single Bragg peak.

Hence, shrinkage at the nanoscale is a complex process consisting of multiple changes to the atomic structure of the gel (i.e., collapse of the interlayer spacing along with local structural rearrangements and changes in silica connectivity), and therefore the extent of shrinkage is more aptly captured from analysis of the PDF data (Figure 4) compared to conventional XRD analysis. Moreover, Pinson *et al*. showed that the maximum macroscopic shrinkage (at low RH) tends to be dominated by strain at the nanoscale (defined as "interlayer" in the article), and our data and subsequent analysis outlined above (Figure 4 and 5) provide more accurate estimates of the magnitude of this shrinkage (0.0027 for C-(N)-A-S-H gel at 0% RH, ~0.0028 for Pinson *et al.* obtained from Figure 6 in ref. 36) without any artificial manipulation of the strain value obtained from X-ray scattering results. Recently, such method of measuring nanoscopic strain from PDF data was used to study the behavior of C-S-H gel under compressive stress, where good agreement between nanoscopic and macroscopic strain was observed.[77] This further demonstrates the suitability of PDF data to measure nanoscopic strain.

Effect of nano-ZrO_2 on drying behavior of C-(N)-A-S-H gel

The susceptibility of cementitious materials to chemical degradation and other stability issues (such as drying-induced shrinkage) has led to researchers experimenting with certain types of nanoparticles with the aim of improving cement performance. For instance, inert nanoparticles have been investigated for their ability to manipulate precipitation and nucleation of the main binder gel during hydration of OPC[44,46] or alkali-activation.[25,45] Here, nano-ZrO_2 is utilized as a potential method to augment the drying-induced atomic structural changes, where it is seen to drastically alter the behavior of silicate-activated slag at an RH of 0% (comparing Figure 6a and Figure 1a). The Ca-T peak in the nano-ZrO_2 sample increases continuously with time as drying progresses, as do the first and second nearest-neighbor Ca-O peaks, which is opposite to the changes seen to occur for the sample without nano-ZrO_2. Unexpectedly, the peak changes in the nano-ZrO_2 sample subjected to drying (Figure 6a) have some resemblance with the difference pattern shown in the silicate-activated slag sample during alkali-activation (Figure 1b and 6b), which is indicative of gel growth. In fact, direct comparison of these difference curves, as given in Figure 7, reveals that there are significant similarities in the two gels (the C-(N)-A-S-H gel that forms during alkali-activation and the "unconventional" gel that precipitates during drying in the sample containing nano-ZrO_2), especially over an r range of ~ 2 – 5 Å. A schematic illustrating such a phenomenon is shown in Figure 8. On the other hand, the impact of nano-ZrO_2 on alkali-activation of the silicate-activated slag (Figure 8a) is minimal, where a comparison of the subtle difference of the evolution of the Ca-T peak can be found in the ESI (Figure S7). Furthermore, as shown in the ESI (Figure S9), the changes seen in the PDF data in Figure 6a are attributed to the atomic structural changes occurring in silicate-activated slag as opposed to separate atom-atom contributions coming from the nano-ZrO_2.

474

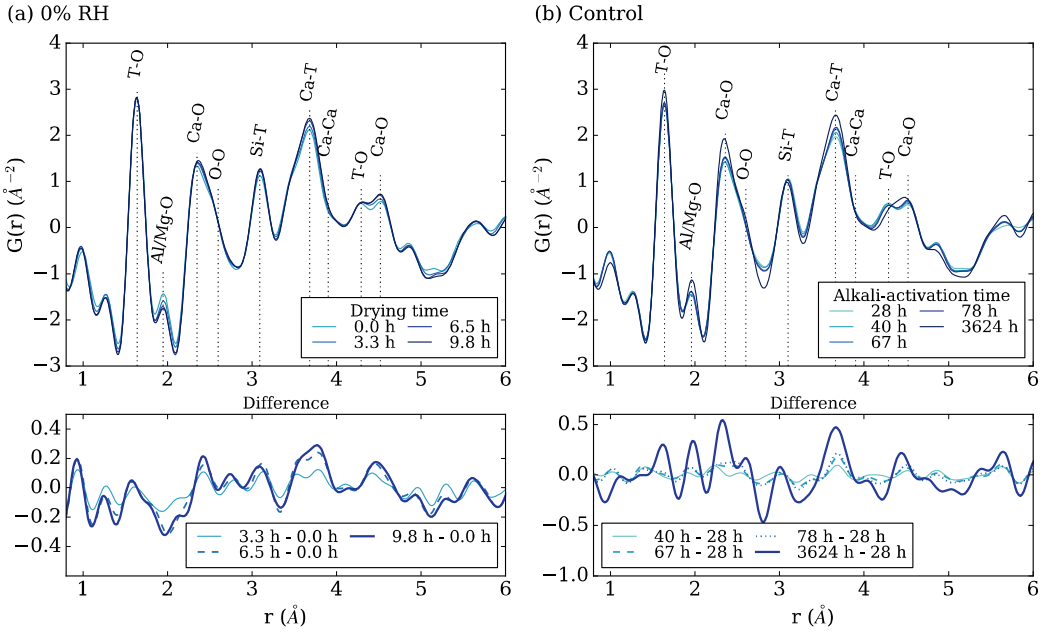

475

476 Figure 6. Synchrotron X-ray PDF curves of silicate-activated slag with nano-ZrO_2 subjected to
477 0% RH (a), and during the alkali-activation reaction (b, denoted as "control"). PDF curves at
478 different times during drying/alkali-activation (top), and difference curves of the PDF data
479 obtained via subtraction of the initial PDF data set (bottom).

480

481 It is observed in Figure 6a that the Si-T peak increases, which is not the case for silicate-
482 activated slag samples undergoing alkali-activation (Figure 1b). This atom-atom correlation
483 denotes the Si-O-T linkages in the (alumino)silica chains, and therefore, an increase in this peak
484 implies that more Si-O-T linkages form, leading to a higher degree of polymerization for the
485 precipitated "unconventional" gel. A similar behavior is seen to occur in the nano-ZrO_2 sample
486 exposed to 43% RH nitrogen gas flow, where the Ca-O (first and second nearest-neighbor), Ca-T
487 and Si-T peaks increase as drying progresses (Figure S2b in the ESI).

488

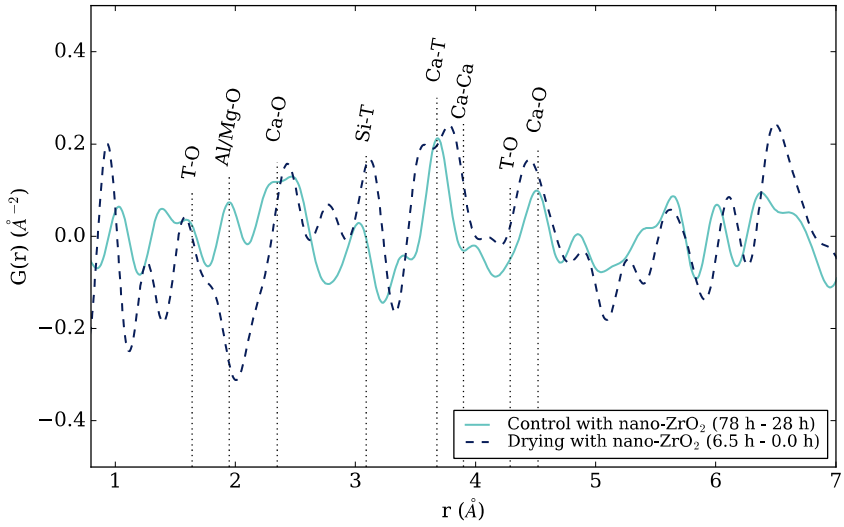

Figure 7. Comparison of the selected difference PDF curves of the silicate-activated slag at 0% RH ("6.5 h – 0.0 h") and in the control environment ("78 h – 28 h") in Figure 6. "0.0 h" indicates the start of drying, where the sample has been cured for 24 hours. "28 h" means that the sample has been cured for 28 hours.

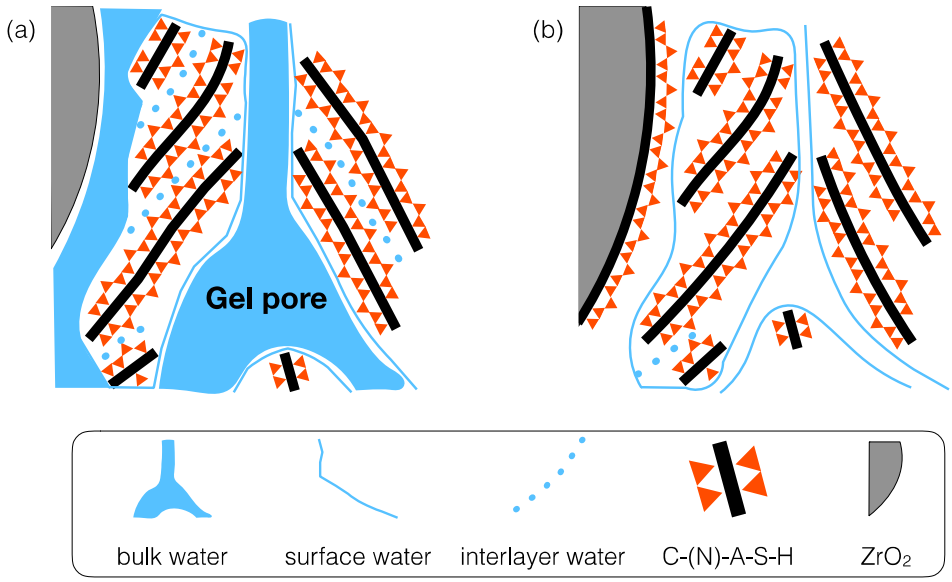

Figure 8. Schematic diagrams of C-(N)-A-S-H gel with nano-ZrO_2 subjected to different RH at the nanoscale (~ 10 nm). (a) In the control environment, and (b) at 43% and 0% RH where there is additional gel growth on the surface of nano-ZrO_2.

Kinetics of local structural changes

To better visualize the changes occurring in the local atomic structure of silicate-activated slag with nano-ZrO_2 during drying, and to enable direct comparison with the no nano data given in Figure 2, the PDF peak intensities of the two atom-atom correlations, Si-T and Ca-T, are normalized with respect to T-O peak and plotted against time (Figure 9). Comparing Figure 2 and 9 reveals that the behavior of silicate-activated slag with nanoparticles is in stark contrast with the sample without nanoparticles. The normalized Si-T and Ca-T peak intensities are now seen to increase continuously for both 0% and 43% RH environments. Moreover, the extent of increase is much larger than that seen for the control silicate-activated slag sample during alkali-activation, which, specifically for the (Si-T)÷(T-O) ratio, indicates that the "unconventional" gel

that precipitates during drying in these systems has a higher degree of polymerization compared with C-(N)-A-S-H gel.

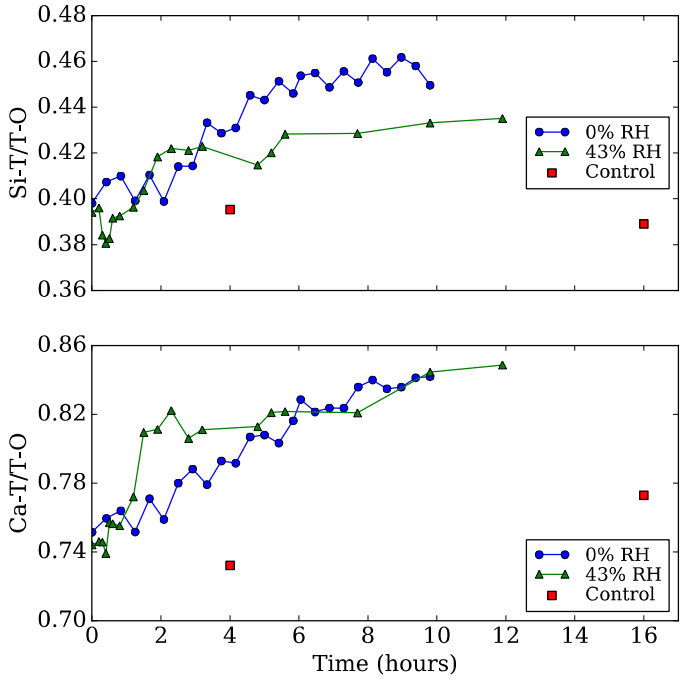

Figure 9. Evolution of normalized Si-T (at ~3.1 Å) and Ca-T (at ~3.65 Å) peak intensities of silicate-activated slag with nano-ZrO_2 at 0% RH, 43% RH and in the control (sealed) environments, all normalized with respect to the T-O peak intensity at ~1.65 Å.

Unlike the case of silicate-activated slag without nanoparticles in the 43% RH environment, where the Si-T and Ca-T atom-atom correlations behave similarly to those of the control sample in the sealed environment (Figure 2), the behavior of the Si-T and Ca-T correlations of silicate-activated slag with nano-ZrO_2 in the 43% RH environment is closer to that of the 0% RH environment (Figure 9). Specifically, the normalized Ca-T peak intensities of silicate-activated

slag with nano-ZrO_2 at 0 and 43% RH essentially overlap while the evolution of the normalized Si-T peak intensity of the silicate-activated slag with nanoparticles in the 43% RH environment lies in between that of the silicate-activated slag with nanoparticles in the 0% RH environment and that in the sealed (control) environment. These data show that growth of the "unconventional" C-(N)-A-S-H gel in the silicate-activated slag with nanoparticles occurs even in a moderately dry environment (43% RH).

As seen in Figure 9, the 0% and 43% RH drying experiment was terminated at ~10 and 12 hrs, respectively, determined at the time of measurement by the plateau in the normalized Si-T peak. However, it turns out that the normalized Ca-T peak is still increasing after 10 hrs, indicating that the "unconventional" gel growth mechanism is ongoing. From comparison of Figure 2 and 9 it can be seen that most of the changes occur during the initial 2 hrs for the samples without nanoparticles, while changes are more uniform across the entire measurement time for the samples with nanoparticles (~ 10 hrs for 0% RH case and ~ 12 hrs for 43% RH case). Furthermore, a subsequent weight loss experiment (Figure S10 in ESI) revealed that the evaporation rates of water in both silicate-activated slag with and without nano-ZrO_2 are similar, indicating that the continual "unconventional" gel growth in silicate-activated slag with nano-ZrO_2 cannot be attributed to the retention of water and therefore the ongoing hydration reaction. Given this, we propose that the continual growth of "unconventional" gel in the silicate-activated slag with nanoparticles is likely associated with the surface reactivity of the nanoparticles, as explained in detail later in this article.

Strain at the nanoscale

The impact of nano-ZrO_2 on the development of nanoscopic strain during drying is shown in Figure 10, where the associated PDF data are given in Figure S6 in the ESI. These data show that nano-ZrO_2 augment the mechanisms occurring at the nanoscale during drying, and therefore mitigate the development of drying-induced shrinkage strains that were previously seen to develop in the sample without nanoparticles (Figure 5). For instance, where a shrinkage strain of 0.0027 developed in the sample without nanoparticles at 0% RH (Figure 5), there is a corresponding expansion strain of 0.0007 for the nano-ZrO_2 sample (Figure 10). Although some PDF peaks of the nano-ZrO_2 samples (Figure S6) shift considerably (e.g., at 11.1 and 13.3 Å for the 0% RH condition and at 13.3 and 20.3 Å for the 43% RH condition), the majority of them show only minimal change, and some of the exceptionally large values are actually artifacts due to the difficulty in describing the complex peak shape (e.g., at 20.3 Å for the 43% RH condition), as can be seen in Figure S6 in the ESI.

The small expansive strain values in the silicate-activated slag with nano-ZrO_2 at 0% RH indicate minimal structural rearrangements in the existing C-(N)-A-S-H gel, possibly due to the reinforcing effect of the "unconventional" gel that precipitates during drying. This interpretation is also supported by the diffraction data (Figure S4b and S5b) where no shift in basal spacing is observed in silicate-activated slag with nano-ZrO_2 for both the 0% and 43% RH conditions. Although water is being pulled out the C-(N)-A-S-H gel in the nano-ZrO_2 samples during drying (as confirmed by the similar weight loss curves in Figure S10 in the ESI), at 0% RH there is no collapse of the interlayer spacing, and therefore the nanoparticles are providing some sort of reinforcing effect to the C-(N)-A-S-H gel.

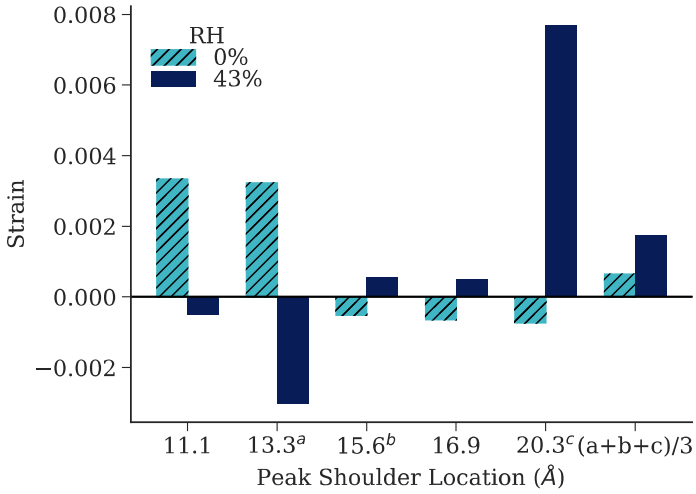

Figure 10. Quantification of the peak shifts in the PDF for silicate-activated slag with nano-ZrO_2 (Figure S6), given as strain values. A positive strain value indicates a shift of the peak shoulder towards larger atomic distances.

Nano-ZrO_2 catalyzing additional gel growth during drying?

Given the significant impact nano-ZrO_2 has on structural rearrangements/changes that occur during drying, we propose that the surface reactivity of the nanoparticles plays a large role in mitigating drying-induced changes. As water molecules evaporate from silicate-activated slag the ionic concentration of the pore solution will increase. However, for the case of silicate-activated slag without nanoparticles, nucleation of additional C-(N)-A-S-H gel does not occur since local supersaturation levels are not reached. It is known that the pH of the pore solution in the silicate-activated slag paste is around 13.[39] Hence, the surface of the nano-ZrO_2 in contact with the pore solution will be electronegative, since the point of zero charge (pzc) for tetragonal zirconia is around 6.7.[78] These negatively charged surfaces associated with the nanoparticles will

584 lead to adsorption of the calcium cations from the pore solution. A similar phenomenon has been
585 reported to occur on the surface of rutile (titanium oxide).[79] It is likely that at higher ionic
586 concentrations (more aggressive drying conditions), the negatively charged silicate and
587 aluminate ions in the pore solution will also adsorb to the surface of the nano-ZrO_2 (attracted to
588 the positively charged calcium ions), leading to growth of a gel. In fact, growth of C-S-H gel on
589 various nanomaterials has been observed using transmission electron microscopy.[80] PDF data for
590 the alkali-activation of silicate-activated slag containing nano-ZrO_2 show that the nanoparticles
591 remain stable in the alkaline pore solution up to 131 days (Figure S11 in the ESI), and therefore
592 reactive zirconia surface will be available throughout the drying period.
593
594 Interestingly, nano-ZrO_2 does not appear to cause the same type of gel growth in silicate-
595 activated slag during the normal alkali-activation reaction, since the PDF data for the silicate-
596 activated slag with (Figure 6b) and without nano-ZrO_2 (Figure 1b) as alkali-activation proceeds
597 are essentially the same. Hence, the nanoparticles remain inert during alkali-activation, and it is
598 possible that only once the degree of solvation of the ZrO_2 nanoparticles drops below a certain
599 level does the surface reactivity become important. It is also interesting to note that this
600 mechanism does not occur in silicate-activated slag without nano-ZrO_2 under drying condition
601 (see Figure 2 and Figure 9), even though there should be an increase in the ionic concentration in
602 these samples. This is due to the fact that the zirconia surface has a higher affinity for binding
603 with ions from the pore solution compared with surfaces that already exist in the silicate-
604 activated slag system (e.g., slag grains, C-(N)-A-S-H gel and hydrotalcite-like phase), such that
605 the growth of the new type of gel in silicate-activated slag with nano-ZrO_2 reinforces the

606 nanoscale structure and prevents damage to the original C-(N)-A-S-H gel as water is removed
607 from the sample.
608
609 To assess the validity of the proposed mechanism, the interactions between silicate monomeric
610 ions, i.e., $SiO(OH)_3^-$, and C-(N)-A-S-H gel (modeled as 14Å tobermorite) or tetragonal zirconia
611 have been studied using DFT. 14Å tobermorite with a chemical formula of
612 $Ca_5Si_6O_{16}(OH)_2 \cdot 7H_2O$ was used for modeling the C-(N)-A-S-H gel surface. The optimized bulk
613 structure of 14Å tobermorite[81] was cut parallel to the *001* surface. Two different 14Å tobermorite
614 surfaces were studied. For the first case, 14Å tobermorite was cleaved through the interlayer
615 region such that a silica-rich surface was obtained. For the second case, 14Å tobermorite was
616 cleaved through the intralayer Ca-O bonds to obtain a surface that was decorated with calcium
617 atoms. The ground state configurations of the surfaces were relaxed after cutting them from the
618 bulk 14Å tobermorite. Following the surface relaxations, silicate ions were allowed to interact
619 with both of these surfaces, with the most favorable bonding configuration on each surface
620 determined via calculation of the minimum total energy. A similar analysis was carried out for
621 tetragonal zirconia that was cleaved along its *111* surface. Here, tetragonal zirconia was chosen
622 because the PDF of the nano-ZrO_2 solution was found to match tetragonal zirconia (see Figure
623 S9 in ESI). Zirconia was cleaved along the *111* surface since it was previously shown to be
624 energetically the most stable surface of tetragonal zirconia.[82] In order to investigate the effect of
625 calcium atoms on the binding of silicate to the surfaces, this process was simulated both with a
626 bare zirconia surface and with a calcium decorated zirconia surface. It should be noted that
627 calcium atoms have been hydrated with five water molecules per unit-cell to begin with for the
628 model C-(N)-A-S-H gel and zirconia.

For each structure, we calculated the binding energy E_b of the silicate ion to the surfaces mentioned above from the expression $E_b = E_T[silicate] + E_T[surface] - E_T[silicate + surface]$, where $E_T[silicate], E_T[surface], and\ E_T[silicate + surface]$ are the total energy of a silicate ion, the surface and the optimized total energy of one silicate ion adsorbed to the surface, respectively. In our notation, $E_b > 0$ indicates that binding of the ion is favorable. All of the total energies were calculated using the same sized slab-based supercell for each structure. Unit-cells for the slabs had dimensions of 12.92 Å × 14.56 Å for 14Å tobermorite and 10.10 Å × 12.25 Å for zirconia in the horizontal ($a \times b$) plane. This corresponds to a separation of 12.92 Å and 12.25 Å between silicates adjacently adsorbed on the surfaces. In the direction perpendicular to the surface (c-axis), a vacuum of 20 Å was chosen in order to avoid interaction between repeating unit-cells.

Our results show that the silicate ion binds to both the silica-cleaved C-(N)-A-S-H gel (3.76 eV) and zirconia (3.99 eV) surfaces (Figure 11a), and these binding energies increase in the presence of hydrated calcium atoms (4.76 eV for Ca-rich C-(N)-A-S-H and 8.69 eV for Ca-rich zirconia surface, Figure 11b), especially for the case of zirconia. Hence, calcium ions are seen to play a crucial role during chemisorption of silicate ions on these surfaces. Furthermore, for both cases (bare surfaces and Ca-decorated), silicate ions are attracted much more strongly to the zirconia surface compared to C-(N)-A-S-H. We repeated the calcium decoration of the surfaces without hydration to ensure that the large increase in binding energy for the zirconia surface is not solely attributed to the presence of water molecules. The binding energies of the silicate ions on the dehydrated Ca-rich surfaces (3.85 eV for C-(N)-A-S-H gel, 7.22 eV for zirconia) are seen to be

almost as large as those for the hydrated case. Hence, these DFT results strongly support our hypothesis that the presence of zirconia nanoparticles in the silicate-activated slag sample act as templates for additional (and "unconventional") gel growth during drying. For the formation of such "unconventional" gel to occur, two factors are necessary: an increased ionic concentration in the pore solution of the silicate-activated slag, and the presence of highly reactive surfaces such as nano-ZrO_2.

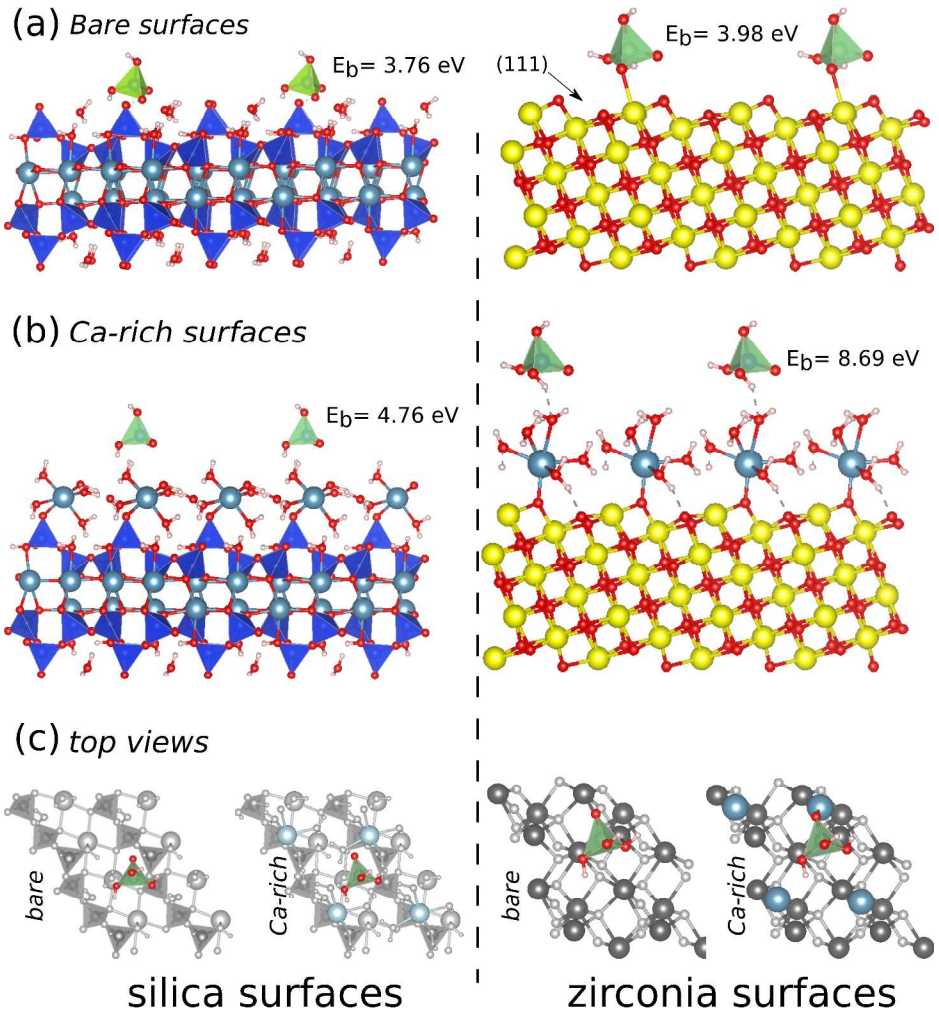

Figure 11. (a) Side views of the optimized geometries of $SiO(OH)_3^-$ ion adsorbed on 14Å tobermorite (denoted as "silica", model for C-(N)-A-S-H gel) and tetragonal zirconia surfaces,

662 shown on left and the right panels, respectively. (b) Same for Ca-rich hydrated surfaces. (c) Top
663 views showing the growth of a new silica layer on the surfaces. Si, Ca, Zr, O, and H atoms are
664 represented by dark blue, cyan, yellow, red and pink spheres in the ball-and-stick model,
665 respectively. For the top views, the layers that are underneath the top most silica tetrahedrons are
666 shown in gray.

667

668 The elucidation of the mechanism reported in this article opens a new pathway to address the
669 long-standing problem of drying-induced microcracking in silicate-activated slag and other
670 materials susceptible to drying-induced cracking. By adding a small amount of zirconia
671 nanoparticles, the silicate-activated slag becomes denser due to additional gel growth during
672 drying, minimizing the extent of nanoscopic shrinkage strain, and therefore potentially making it
673 more resistant to microcracking. However, the nanoparticles should be chosen carefully, as
674 recent studies have shown mixed effects on silicate-activated slag depending on the type of
675 nanoparticles selected.[83,84] The impact of nano-ZrO_2 on other cementitious systems (e.g., OPC
676 and alkali-activated metakaolin/fly ash and colloids/ceramics) is also worth investigating, since
677 robust mitigation routes are needed for these crack-prone materials.

678

679 # Conclusions

680 The drying-induced atomic structural changes in sodium-based silicate-activated slag with and
681 without zirconia nanoparticles have been investigated using synchrotron X-ray pair distribution
682 function (PDF) analysis and density functional theory (DFT) calculations. For the case without
683 nanoparticles, the PDF data contain direct information on the development of nanoscopic strain

in silicate-activated slag during drying. This strain is caused by two concurrent mechanisms: (1) partial collapse of the interlayer spacing, and (2) slight disintegration of the C-(N)-A-S-H gel leading to breakage of Ca-O-T and Si-O-T linkages and formation of smaller nanosized domains. These findings help bridge the knowledge gap on the nanoscopic shrinkage mechanisms that are contributing to macroscopic length changes in the C-S-H-like systems. Moreover, this investigation has shown that the addition of a small amount of nano-ZrO_2 (~ 0.17 wt. %) drastically alters the drying-induced behavior of silicate-activated slag, where an "unconventional" silica-rich gel is seen to precipitate as drying progresses, which provides a reinforcing effect and minimizes the development of nanoscopic strain. Hence, the zirconia surfaces are catalyzing additional gel growth during drying, where an increase in the ionic concentration of the pore solution leads to the precipitation of a highly polymerized silica gel on the surface of the nanoparticles. This proposed mechanism is supported by DFT calculations of the binding energy between a negatively charged silicate monomer and various configurations for C-(N)-A-S-H gel and zirconia surfaces. Irrespective of the hydration state and whether Ca ions are adsorbed to the surfaces, the silicate monomer is found to bind more strongly to zirconia. Therefore, this investigation opens potential pathways for the development of new and novel solutions to the long-standing problem of drying shrinkage in sustainable cements and other porous materials.

Conflicts of interest

There are no conflicts to declare.

Acknowledgments

This work was supported by NSF through the MRSEC Center (Grant No. DMR-1420541). KG was supported by NSF, Grant No. CMMI-1362039, and NG and VOO were funded by the Andlinger Center for Energy and the Environment (Princeton University). The authors would like to thank Mr. Kevin Beyer and Dr. Olaf Borkiewicz for their assistance with the experiment setup at the Advanced Photon Source (APS). Use of the APS at Argonne National Laboratory was supported by the U. S. Department of Energy, Office of Science, Office of Basic Energy Sciences, under Contract No. DE-AC02-06CH11357. The calculations presented in this article were performed on computational resources supported by the Princeton Institute for Computational Science and Engineering (PICSciE) and the Office of Information Technology's High Performance Computing Center and Visualization Laboratory at Princeton University. The authors thank Dr Jie Feng for his help in conducting the dynamic light scattering experiment.

References

1 G. W. Scherer, *J. Am. Ceram. Soc.*, 1990, **73**, 3–14.

2 K. B. Singh and M. S. Tirumkudulu, *Phys. Rev. Lett.*, 2007, **98**, 218302.

3 H. Yang, Q. Shi, B. Tian, S. Xie, F. Zhang, Yan, B. Tu and D. Zhao, *Chem. Mater.*, 2003, **15**, 536–541.

4 D. Bellet and L. Canham, *Adv. Mater.*, 1999, **10**, 487–490.

5 E. Worrell, L. Price, N. Martin, C. Hendriks and L. O. Meida, *Annu. Rev. Energy. Environ.*, 2001, **26**, 303–329.

6 P. Duxson, J. L. Provis, G. C. Lukey and J. S. J. van Deventer, *Cem. Concr. Res.*, 2007, **37**,

1590–1597.

7 B. C. McLellan, R. P. Williams, J. Lay, A. van Riessen and G. D. Corder, *J. Cleaner Prod.*, 2011, **19**, 1080–1090.

8 J. S. J. van Deventer, J. L. Provis and P. Duxson, *Miner. Eng.*, 2012, **29**, 89–104.

9 P. Duxson and J. L. Provis, *J. Am. Ceram. Soc.*, 2008, **91**, 3864–3869.

10 A. Hajimohammadi, J. L. Provis and J. S. J. van Deventer, *Ind. Eng. Chem. Res.*, 2008, **47**, 9396–9405.

11 J. L. Provis and S. A. Bernal, *Annu. Rev. Mater. Res.*, 2014, **44**, 299–327.

12 P. Duxson, A. Fernández-Jiménez, J. L. Provis, G. C. Lukey, A. Palomo and J. S. J. van Deventer, *J. Mater. Sci.*, 2006, **42**, 2917–2933.

13 J. L. Bell, P. E. Driemeyer and W. M. Kriven, *J. Am. Ceram. Soc.*, 2009, **92**, 1–8.

14 A. Blyth, C. A. Eiben, G. W. Scherer and C. E. White, *J. Am. Ceram. Soc.*, 2017, **100**, 4848–4859.

15 A. E. Morandeau and C. E. White, *Chem. Mater.*, 2015, **27**, 6625–6634.

16 S. A. Bernal, R. San Nicolas, R. J. Myers, R. Mejía de Gutierrez, F. Puertas, J. S. J. van Deventer and J. L. Provis, *Cem. Concr. Res.*, 2014, **57**, 33–43.

17 S. A. Bernal, J. L. Provis, D. G. Brice, A. Kilcullen, P. Duxson and J. S. J. van Deventer, *Cem. Concr. Res.*, 2012, **42**, 1317–1326.

18 F. Puertas, M. Palacios and T. Vázquez, *J. Mater. Sci.*, 2006, **41**, 3071–3082.

19 T. Bakharev, J. G. Sanjayan and Y. B. Cheng, *Cem. Concr. Res.*, 2002, **32**, 211–216.

20 J. Aliques-Granero, T. M. Tognonvi and A. Tagnit-Hamou, *Mater. Struct.*, 2017, **50**, 36.

21 I. Ismail, S. A. Bernal, J. L. Provis, S. Hamdan and J. S. J. van Deventer, *Mater. Struct.*, 2013, **46**, 361–373.

22 T. Bakharev, *Cem. Concr. Res.*, 2005, **35**, 1233–1246.

23 S. A. Bernal, J. L. Provis, V. Rose and R. Mejía de Gutierrez, *Cem. Concr. Compos.*, 2011, **33**, 46–54.

24 C. Cartwright, F. Rajabipour and A. Radlińska, *J. Mater. Civ. Eng.*, 2015, **27**, B4014007.

25 L. Y. Yang, Z. J. Jia, Y. M. Zhang and J. G. Dai, *Cem. Concr. Compos.*, 2015, **57**, 1–7.

26 A. A. Melo Neto, M. A. Cincotto and W. Repette, *Cem. Concr. Res.*, 2008, **38**, 565–574.

27 F. Collins and J. G. Sanjayan, *Cem. Concr. Res.*, 2000, **30**, 1401–1406.

28 G. W. Scherer, J. J. Valenza II and G. Simmons, *Cem. Concr. Res.*, 2007, **37**, 386–397.

29 M. C. Garci Juenger and H. M. Jennings, *Cem. Concr. Res.*, 2001, **31**, 883–892.

30 I. Ismail, S. A. Bernal, J. L. Provis, S. Hamdan and J. S. J. van Deventer, *J. Mater. Sci.*, 2013, **48**, 3566–3577.

31 R. F. Feldman and J. J. Beaudoin, *Cem. Concr. Res.*, 1991, **21**, 297–308.

32 S. Diamond, *Cem. Concr. Res.*, 2000, **30**, 1517–1525.

33 W. Hansen, *J. Am. Ceram. Soc.*, 1987, **70**, 323–328.

34 Q. Zeng, K. Li, T. Fen-chong and P. Dangla, *Cem. Concr. Res.*, 2012, **42**, 194–204.

35 G. W. Scherer, *Transp. Porous Media*, 2015, **110**, 311–331.

36 M. B. Pinson, E. Masoero, P. A. Bonnaud, H. Manzano, Q. Ji, S. Yip, J. J. Thomas, M. Z. Bazant, K. J. Van Vliet and H. M. Jennings, *Phys. Rev. Appl.*, 2015, **3**, 064009.

37 P. A. Bonnaud, Q. Ji, B. Coasne, R. J. M. Pellenq and K. J. Van Vliet, *Langmuir*, 2012, **28**, 11422–11432.

38 I. Maruyama, Y. Nishioka, G. Igarashi and K. Matsui, *Cem. Concr. Res.*, 2014, **58**, 20–34.

39 X. Cong and R. J. Kirkpatrick, *Cem. Concr. Res.*, 1995, **25**, 1237–1245.

40 C. E. White, L. L. Daemen, M. Hartl and K. Page, *Cem. Concr. Res.*, 2015, **67**, 66–73.

41 A. Kudo, S. A. Steiner III, B. C. Bayer, P. R. Kidambi, S. Hofmann, M. S. Strano and B. L. Wardle, *J. Am. Chem. Soc.*, 2014, **136**, 17808–17817.

42 S. A. Steiner III, T. F. Baumann, B. C. Bayer, R. Blume, M. A. Worsley, W. J. MoberlyChan, E. L. Shaw, R. Schlögl, A. J. Hart, S. Hofmann and B. L. Wardle, *J. Am. Chem. Soc.*, 2009, **131**, 12144–12154.

43 Singh, L.P., S. K. Bhattacharyya, S. P. Shah, G. Mishra, S. Ahalawat and U. Sharma, *Constr. Build. Mater.*, 2015, **74**, 278–286.

44 S. Kawashima, P. Hou, D. J. Corr and S. P. Shah, *Cem. Concr. Compos.*, 2013, **36**, 8–15.

45 C. A. Rees, J. L. Provis, G. C. Lukey and J. S. J. van Deventer, *Colloids Surf., A*, 2008, **318**, 97–105.

46 J. M. Makar and G. W. Chan, *J. Am. Ceram. Soc.*, 2009, **92**, 1303–1310.

47 A. R. Jayapalan, B. Y. Lee and K. E. Kurtis, *Cem. Concr. Compos.*, 2013, **36**, 16–24.

48 A. Nazari and S. Riahi, *Mater. Res.*, 2010, **13**, 551–556.

49 K. Gong, Z. Pan, A. H. Korayem, L. Qiu, D. Li, F. Collins, C. M. Wang and W. H. Duan, *J. Mater. Civ. Eng.*, 2015, **27**, A4014010.

50 A. M. Rashad, *Constr. Build. Mater.*, 2014, **52**, 437–464.

51 P. J. Chupas, K. W. Chapman, C. Kurtz, J. C. Hanson, P. L. Lee and C. P. Grey, *J. Appl. Crystallogr.*, 2008, **41**, 822–824.

52 P. J. Chupas, X. Qiu, J. C. Hanson, P. L. Lee, C. P. Grey and S. J. L. Billinge, *J. Appl. Crystallogr.*, 2003, **36**, 1342–1347.

53 A. P. Hammersley, *European Synchrotron Radiation Facility Internal Report, ESRF97HA02T*, 1997.

54 A. P. Hammersley, S. O. Svensson and A. Thompson, *Nucl. Instrum. Methods Phys. Res.,*

Sect. A, 1994, **346**, 312–321.

55 T. Egami and S. J. Billinge, *Underneath the Bragg peaks: Structural Analysis of Complex Materials*, Elsevier, Amsterdam, The Netherlands, 2003.

56 X. Qiu, J. W. Thompson and S. J. L. Billinge, *J. Appl. Crystallogr.*, 2004, **37**, 678–678.

57 S. Grimme, *J. Comput. Chem.*, 2006, **27**, 1787–1799.

58 P. E. Blöchl, *Phys. Rev. B*, 1994, **50**, 17953–17979.

59 J. P. Perdew, K. Burke and M. Ernzerhof, *Phys. Rev. Lett.*, 1996, **77**, 3865–3868.

60 G. Kresse and J. Furthmüller, *Phys. Rev. B*, 1996, **54**, 11169–11186.

61 C. E. White, J. L. Provis, T. Proffen and J. S. J. van Deventer, *J. Am. Ceram. Soc.*, 2010, **93**, 3486–3492.

62 Y. Zhang, C. A. Davy, G. Tricot, C. Albert-Mercier, N. Henry, P. Bertier, F. Cazaux, D. Damidot and X. Bourbon, *J. Am. Ceram. Soc.*, 2017, **100**, 4131–4152.

63 A. H. Narten, W. E. Thiessen and L. Blum, *Science*, 1982, **217**, 1033–1034.

64 L. B. Skinner, C. Huang, D. Schlesinger, L. G. M. Pettersson, A. Nilsson and C. J. Benmore, *J. Chem. Phys.*, 2013, **138**, 074506.

65 I. Maruyama, N. Sakamoto, K. Matsui and G. Igarashi, *Cem. Concr. Res.*, 2017, **91**, 24–32.

66 K. Gong and C. E. White, *Cem. Concr. Res.*, 2016, **89**, 310–319.

67 A. E. Morandeau, J. P. Fitts, H. D. Lee, S. M. Shubeita, L. C. Feldman, T. Gustafsson and C. E. White, *Cem. Concr. Res.*, 2016, **79**, 45–48.

68 H. M. Jennings, *Mater. Struct.*, 2004, **37**, 59–70.

69 W. A. Gutteridge and L. J. Parrott, *Cem. Concr. Res.*, 1976, **6**, 357–366.

70 P. Pourbeik, J. J. Beaudoin, R. Alizadeh and L. Raki, *Adv. Cem. Res.*, 2015, **27**, 2–10.

71 B. Bissonnette, P. Pierre and M. Pigeon, *Cem. Concr. Res.*, 1999, **29**, 1655–1662.

72 T. C. Powers, *J. Am. Ceram. Soc.*, 1958, **41**, 1–6.

73 H. M. Jennings and Y. Xi, in *Creep and shrinkage of concrete*, eds. Z. P. Bazant and I. Carol, E & FN Spon, London, 1993, pp. 85–102.

74 Y. Xi and H. M. Jennings, *Mater. Struct.*, 1997, **30**, 329–339.

75 J. J. Thomas, A. J. Allen and H. M. Jennings, *J. Am. Ceram. Soc.*, 2008, **91**, 3362–3369.

76 C. M. Neubauer and H. M. Jennings, *J. Mater. Sci.*, 2000, **35**, 5751–5765.

77 S. Bae, H. Jee, M. Kanematsu, A. Shiro, A. Machida, T. Watanuki, T. Shobu and H. Suzuki, *J. Am. Ceram. Soc.*, 2017, **101**, 408–418.

78 S. Ardizzone and C. L. Bianchi, *J. Electroanal. Chem.*, 1999, **465**, 136–141.

79 N. Lee, D. A. Sverjensky and R. M. Hazen, *Environ. Sci. Technol.*, 2014, **48**, 9358–9365.

80 H. Li, T. Du, H. Xiao and Q. Zhang, *J. Am. Ceram. Soc.*, 2017, **100**, 3227–3238.

81 V. O. Özçelik and C. E. White, *J. Phys. Chem. Lett.*, 2016, **7**, 5266–5272.

82 A. Christensen and E. A. Carter, *Phys. Rev. B*, 1998, **58**, 8050–8064.

83 N. Garg and C. E. White, *J. Mater. Chem. A*, 2017, **5**, 11794–11804.

84 M. H. Hubler, J. J. Thomas and H. M. Jennings, *Cem. Concr. Res.*, 2011, **41**, 842–846.